Cellular events of acute, resolving or progressive COVID-19 in SARS-CoV-2 infected non-human primates

Fahlberg MD[1], Blair RV[1,2], Doyle-Meyers LA[1], Midkiff CC[1], Zenere G[1], Russell-Lodrigue KE[1], Monjure CJ[1,2], Haupt EH[1], Penney TP[1], Lehmicke G[1], Threeton BM[1], Golden N[1], Datta PK[1,2], Roy CJ[1,2], Bohm RP[1,2], Maness NJ[1,2], Fischer T[1,2], Rappaport J[1,2], and Vaccari M[1,2*].

[1]Tulane National Primate Research Center, Covington, LA
[2]Tulane University School of Medicine, New Orleans, LA

*To whom correspondence should be addressed:

Monica Vaccari, Ph.D.

Associate Professor, Tulane National Primate Research Center,

18703 Three Rivers Road, Covington, LA 70433

Email: mvaccari@ tulane.edu

Abstract

We investigated the immune events following SARS-CoV-2 infection, from the acute inflammatory state up to four weeks post infection, in non-human primates (NHP) with heterogeneous pulmonary pathology. The acute phase was characterized by a robust and rapid migration of monocytes expressing CD16 from the blood and concomitant increase in CD16+ macrophages in the lungs. We identified two subsets of interstitial macrophages (HLA-DR+ CD206–), a transitional CD11c+ CD16+ cell population that was directly associated with IL-6 levels in plasma, and one long lasting CD11b+ CD16+ cell population. Strikingly, levels of monocytes were a correlate of viral replication in bronchial brushes and we discovered TARC (CCL17) as a new potential mediator of myeloid recruitment to the lungs. Worse disease outcomes were associated with high levels of cell infiltration in lungs including CD11b+ CD16hi macrophages and CD11b+ neutrophils. Accumulation of macrophages was long-lasting and detectable even in animals with mild or no signs of disease. Interestingly, animals with anti-inflammatory responses including high IL-10:IL-6 and kynurenine to tryptophan ratios had less signs of disease. Our results unravel cellular mechanisms of COVID-19 and suggest that NHP may be appropriate models to test immune therapies.

The COVID-19 pandemic is a major public health crisis, causing a global medical emergency. There are currently no effective vaccines or drugs approved to completely treat or prevent COVID-19, and much remains unknown about the pathogenesis of the disease. COVID-19 presents with highly variable outcomes, and patients that develop symptoms exhibit a wide range of disease, spanning from mild (fever, cough, shortness of breath) to severe (dyspnea,

50 pneumonia, rapidly progressing radiographic changes)[1]. It is currently estimated that up to 15%
51 of COVID-19 patients progress to acute respiratory distress syndrome (ARDS)[2], which is the
52 major cause of death among fatal SARS-CoV-2 cases. Studies elucidating molecular and
53 immunological details of SARS-CoV-2 infection are underway, and many of the reported
54 clinical observations point to the disease being at least partly the result of an excessive host
55 response aimed to clear the virus but instead contributing to disease development[3]. This
56 hypothesis is supported by studies on the closely related coronavirus SARS-CoV-1[4-6], and by
57 clinical reports showing elevated levels of the proinflammatory cytokine IL-6 in SARS-CoV-2
58 infected patients, and profound dysregulation of the myeloid cell compartment, particularly
59 among those with severe symptoms[3,7-9].
60
61 Interestingly, the increase in IL-6 coincides with the upregulation of chemokines responsible for
62 myelopoiesis and monocyte recruitment to the lungs[3,10] suggesting that peripheral inflammatory
63 monocytes and tissue macrophages may play a role in the cytokine storm seen in severe COVID-
64 19 patients[11]. The underlying inflammatory state and increased myelopoiesis seen in older
65 individuals may be responsible for the high mortality rate seen in this group[12]. A better
66 understanding of immunopathology of COVID-19 will aid the development of targeted
67 immunotherapies and effective vaccines.
68
69 Non-human primates (NHP) have been used as animal models to study acute respiratory diseases
70 such as SARS and MERS[13]. In these studies, African green monkeys (AGM) have been shown to
71 be more susceptible to severe disease than rhesus macaques (RM)[14]. Regardless of species
72 differences, and given the overlap between NHP and with human immune systems, both NHP

73 species have been useful models to study host responses to coronaviruses[5]. We and others have
74 shown that both AGM and RM can be successfully infected with SARS-CoV-2 via the intranasal
75 and the intratracheal route, or by aerosol[15-18]. Following exposure, AGM and RM have high
76 levels of virus replication in the respiratory tract for up to two weeks, and both species develop
77 pulmonary pathology characteristic of COVID-19, that varies from very mild to severe[19]. Other
78 groups have described the very early immune events in SARS-CoV-2 infected rhesus macaques,
79 with perturbation of monocytes populations, increased macrophages in lungs, and cellular
80 activation in blood all happening a few days following the infection[16].
81 Here, we extend on these findings by describing the kinetics of immune events following
82 infection, spanning from the acute phase up to four weeks following infection, in the blood and
83 the lungs of four African green monkeys (AGM) and four rhesus macaques (RM) with a
84 heterogeneous spectrum of COVID-19. Overall, we observed a multiphasic mobilization of
85 innate and adaptive cells from the blood to the lung that is strikingly common to both species.
86 The acute inflammatory phase was characterized by an increase in the frequency of monocytes
87 that was positively associated with bronchial viral replication. CD11b+ macrophages and
88 neutrophils were detected in the lungs of all infected animals, however, with greater numbers in
89 severe disease. Consistent with the resolution phase of inflammation in the lung[20], the second
90 phase was characterized by a switch toward type 2 responses in both species. We identified two
91 populations of interstitial macrophages (HLA-DR+ CD206–) in BAL; 1) CD11c+ CD16^{hi}
92 population increasing during the acute phase of infection that was associated with IL-6 levels in
93 the plasma, and 2) a long lasting CD11b+ and CD16^{hi} population accumulating in lungs of both
94 AGM and RM, particularly in those with increased disease severity. Animals with more
95 pronounced clinical signs had a higher level of infiltrates in lungs when compared with animals

96 with no or mild signs, lower IL-10:IL-6 and kynurenine /tryptophan ratios (anti-inflammatory:
97 pro-inflammatory) cytokines in plasma[21]. By investigating temporal and spatial changes in
98 immune cells our study links together findings in both NHP and human patients and unravels
99 new cellular events of COVID-19[22,23]. Further, we show that NHP are highly relevant models to
100 study COVID-19 immunopathology and suggest that they may be appropriate models to test
101 immune therapies and vaccines for SARS-CoV-2.
102

103 ## Results
104
105 **Increased levels of monocytes and chemokines after infection is associated with viral load**
106 **and disease severity.** Four adult RM and four adult AGM were exposed to SARS-CoV-2 by
107 either aerosol or mucosal challenge including buccal, intranasal, intratracheal, and conjunctival
108 (multi-route) exposure (**Supplementary Table 1**). The study concluded at 4 weeks post
109 exposure (**Fig. 1A**)[18]. All eight animals had detectable viral load by RT-PCR on nasal and
110 pharyngeal swabs and bronchial brushes by week 1 (**Fig. 1B**, **Supplementary Table 2**). Viral
111 RNA was also detected in pharyngeal, nasal, buccal, rectal and vaginal swabs. No differences in
112 viral load (VL) were observed between the different routes of exposure or between the two
113 species at week 1 (**Supplementary Table 2 and Fig. 1B**). Of note, by week 2 AGM had higher
114 VL than RM in the bronchial brushes and by week 3 VL in RM was mostly undetectable while it
115 remained above detection levels in AGM until study completion (**Fig. 1B** and **Supplementary**
116 **Table 2**). Similar to humans, the course of disease varied widely across animals, as detailed in
117 **Table 1**. Of the four AGM enrolled, two animals developed severe respiratory signs and were
118 euthanized on days 8 (NC34) and 22 (NC33) post-infection, following established endpoint
119 criteria for NHP study protocols, and as we previously reported[18]. Of the two remaining AGM,

120 NC38 had multifocal mild to moderate interstitial pneumonia scattered throughout all lung lobes
121 and NC40 was mostly asymptomatic and had scant inflammation in all lung lobes at necropsy.
122 Three of the four RM (GH99, HD09, and FR04) developed pneumonia characterized by a
123 granulomatous to pyogranulomatous inflammatory response. This was severe in GH99, mild in
124 HD09, and minimal in FR04. Histopathology of the fourth RM (HB37) revealed a lymphocytic
125 vasculitis and proliferative vasculopathy in the right middle lung lobe.
126 Clinical signs observed during the course of the study included mild tachypnea (day 11) and
127 cough (day 15) in GH99 (**Supplementary Table 3**). Intermittent mild to moderate pyrexia was
128 observed in HB37 (day 1-21 post infection). Radiographic changes included a nodule in the right
129 caudal lung lobe (day 11) in GH99, and HD09 also developed a mild, focal increased opacity in
130 the ventral lung field at day 11 (data not shown).Viral loads in the bronchial alveolar brushes at
131 all time points, temperature, pulse oxygen levels (SpO_2) and ranking did not differ between
132 female (n = 3) and males (n = 5) or between animals exposed to different routes of infection
133 (multi route n = 4 and aerosol n = 4), possibly due to the small number of animals per group
134 (**Supplementary Table 2 - 4**).
135 Viral load was not significantly associated with pulmonary pathology, however we observed an
136 inverse association between viral load at week 1 and disease severity ranking (1 to 8 from most
137 severe to least severe) based on the above observations and histopathology findings (AGM: R =
138 0.8 ; RM: R = –0.4, all animals: P = 0.057, R = – 0.71, by the Spearman correlation test) (**Fig.
139 1C**, **Supplementary Fig. 1A** and **1B** (**Supplementary Table 5**).
140
141 Interestingly, virus-driven immunological changes were remarkably similar between species at
142 this time (**Fig. 1** and **Supplementary Fig. 1**). To investigate overall changes driven by viral

143 replication in both groups, we combined their immunological analysis, however at the same time
144 we maintained different specifications for each species (teal = RM and magenta = AGM). Data
145 and statistics are also shown separately per group in **Supplementary Figure 1**. At 1 week after
146 infection both AGM and RM had an increase in the absolute number and frequency of
147 monocytes in the blood (P = 0.065, and P = 0.02 respectively, by the Tukey multiple comparison
148 test, n = 8) compared to baseline levels (**Fig. 1D** and **1E**). This change was significant in AGM
149 alone (absolute number: P = 0.0006, n = 4), and was also observed in all RM, particularly GH99
150 (**Supplementary Fig. 1C - 1F)**. Of note, the increase in absolute number of monocytes remain
151 significant when GH99 was removed from the statistical analysis (P = 0.00002, **Supplementary**
152 **Fig. 1G**). The absolute number of neutrophils in blood did not change over time
153 (**Supplementary Fig. 1H**). Interestingly, the absolute number of monocytes at week 1 was
154 strongly positively associated with the viral load levels in the bronchial brush samples (P =
155 0.002, R = 0.93 by the Spearman test) when all the animals were combined (**Fig. 1F**) (AGM: R =
156 0.8; R: R = 1, not significant in separated groups, **Supplementary Fig. 1I** and **1J**), and remained
157 significant when GH99 was removed from the statistical analysis (**Supplementary Fig. 1K**).
158 We then used the CD14 and CD16 markers to discriminate between three circulating monocytes
159 subtypes: classical (CD14hi CD16low), intermediate (CD14hi CD16hi) and non-classical
160 (CD14low CD16hi) within the total (CD45, live , HLA-DR+ CD16hi) monocyte population by
161 flow cytometry (**Fig. 1G - 1I** and **Supplementary Fig. 2**). Subsets were gated as shown in
162 **Supplementary Figure 2A**, using a strategy that excludes CD16+ NK cells that are negative for
163 HLA-DR[24]. At week 1, the frequency of classical monocytes was significantly increased in
164 blood, as seen in humans[25], and the non-classical population was profoundly depleted (increased
165 levels baseline versus week 1: classical P = 0.007 and decreased non-classical P = 0.005 in all

166 animals combined, n = 4) (**Fig. 1H** and **1I**, and **Supplementary Fig. 2B – 2E**). As we observed
167 for the frequency, the absolute counts of classical and non-classical monocytes at week 1 were
168 also significantly increased and decreased, respectively, compared to the baseline values
169 (**Supplementary Figure 2F - G**). Interestingly, pre infection levels were never completely
170 restored even after 3 weeks post-infection (week 1 vs. week 3: classical P = 0.03 and non-
171 classical P = 0.03), as the number of circulating CD16hi monocytes increased overtime (non-
172 classical week 1 versus week 3: P = 0.0019). These results suggest emerging myelopoiesis and
173 rapid and robust recruitment of patrolling monocytes in tissues following infection in both
174 species. We did not observe changes in the frequency or number of intermediate monocytes
175 (**Supplementary Fig. 2H** and **2I**). In line with what we observed for the total monocyte count, at
176 week 1 the counts for the subsets of monocytes were positively associated with viral replication
177 detected at the bronchial alveolar sites (classical: R = 0.98; P = 0.06, non-classical: R = 0.96; P =
178 0.03 and intermediate R = 0.94; P = 0.06, by the Pearson test), further suggesting that the robust
179 myelopoiesis is therefore driven by the virus in the lung. Within the total monocytes, the
180 frequency of non-classical monocytes was significantly associated with lower viral loads
181 (classical: R = -0.9867; P = 0.0133, by the Pearson Test, adjusted for multiple comparison P =
182 0.07). It is important to note that none of these analyses were significant when the values were
183 adjusted for multiple comparisons (**Supplementary Table 6**).
184 Recent studies in humans have described an increase in the frequency of CD14 positive cells
185 expressing low levels of HLA-DR in COVID-19 patients. These cells phenotypically resemble
186 suppressive subsets of myeloid derived suppressor cells (MDSCs)[8] thus they may decrease
187 disease driven inflammation. We and others have previously identified MDSCs in blood of
188 monkeys by flow cytometry as HLA-DR^{low} CD14^{hi} cells within the CD45/live population[26,27].

189 Some of the animals in our study showed increased MDSCs frequency at week 3 compared to
190 baseline levels, however these changes were not significant (**Supplementary Fig. 2L**). We
191 measured Arginase 1 activity as a functional assay to assess the function of immunosuppressive
192 myeloid cells at the same time points (baseline and week 3) and we did not observe significant
193 changes in plasma overtime (**Supplementary Fig. 2M**)[28].
194
195 We analyzed a group of eight chemokines known to be involved in the mobilization of innate
196 cells, including monocytes, from the blood to the lung: IP-10 (CXCL-10), MCP-1 (CCL2),
197 MCP-4 (CCL13), Eotaxin, TARC (CCL17), MDC (CCL22), MIP-1α and MIP-1β
198 (**Supplementary Fig 3A - 3H**). Some of the chemokines measured at baseline in plasma differed
199 between the two species (MCP-4, Eotaxin, MIP-1b and MDC) as shown by the principle
200 component analysis in S**upplementary Fig. 3I** (**Supplementary Tables 7 - 9**). Plasma levels of
201 TARC (CCL17), a ligand for CCR4 that is involved in Th2 cell recruitment[29], were strongly
202 associated with the frequency of monocytes in blood (P = 0.003, R = 0.95, Spearman test,
203 adjusted for multiple comparison: P = 0.02) (**Fig. 1J**). Similarly, TARC/CCL17 was also
204 associated with viral replication in BAL at week 1 (**Fig. 1K** and **Supplementary Fig. 3J** and
205 **3K**) (P = 0.02, R = 0.857, adjusted for multiple comparisons: P = 0.2, and R = 0.927 and P=
206 0.016 when GH99 is excluded from the analysis), as was IP-10 (P = 0.05, R = 0.78, adjusted for
207 multiple comparisons) when all animals were grouped together (**Fig. 1K** and **Supplementary**
208 **Fig. 3L**), a ligand for CXCR3 that is associated with disease severity and predicts progression of
209 COVID-19 in humans[30]. To gain a better understanding of a common milieu possibly driving
210 monocyte migration observed in both groups we analyzed changes in the levels of these markers
211 with respect to the baseline (**Fig. 1L** and **Supplementary Table 8**). Overall this analysis

212 revealed that animals with the most severe disease outcomes had higher levels of chemokines at
213 week 1, including IP-10, TARC (CCL17).
214
215 **Myelomonocytic cells infiltrate BAL and are associated with IL-6.** Influx of macrophages has
216 been observed in the lung of severe cases of COVID-19 in humans[31]. To monitor cell trafficking
217 into the lungs, we collected bronchoalveolar lavage (BAL) at baseline and after each week
218 following infection, up to week 3. As expected, the majority of the cells found in BAL at
219 baseline were alveolar macrophages (AM)[32]. These cells are readily identified by the mannose
220 receptor C type 1 (CD206) marker, express high levels of HLA-DR, and are positive for the
221 scavenger receptor CD163 (**Fig. 2, Supplementary Fig. 4A** and **4B**), we observed a decrease in
222 the proportion of AM at week 1 post infection in animals of both species, corresponding with an
223 influx of myeloid HLA-DR+ CD206– CD163– cells (**Fig. 2A** and **2B**, **Supplementary Fig. 4C**).
224 Levels of AM similar to pre-infection were restored at week 2 in all but one animal (GH99), and
225 a concomitant increase of CD86 mean fluorescent intensity (MFI) in this population was
226 observed suggesting an M1 activation state[33] (**Supplementary Fig. 4D**). An increase was also
227 seen in the frequency of CD206+ CD163–that have been previously described as endothelial
228 cells which facilitate lymphocyte trafficking and they are detectable in BAL during inflammatory
229 events (**Fig. 2C**)[34].
230 T-distributed stochastic neighbor embedding (tSNE) analysis revealed changes in the phenotype
231 of CD16, CD11b, and CD11c positive populations most prominently at 1-2 weeks post infection
232 (**Fig. 2D - 2F**). In contrast to what we observed in the blood, there was an increase of CD16+
233 HLA-DR+ cells in BAL over time (**Fig. 2G**, and **Supplementary Fig. 4E** and **4F**). We observed
234 a transient increase in the level of CD11c+ CD16+ myelomonocytic cells, which function has
235 been described as patrolling, and they participate in rapid tissue invasion and monocyte survival

236 (baseline vs. week 1: P = 0.015) (**Fig. 2H**)[35,36]. The frequency of CD11c+ macrophages in BAL
237 at week 3 was strongly associated with the levels of the proinflammatory IL-6 cytokine in the
238 plasma at the same time point (week 3: P = 0.003, R = 0.96, Spearman test) (**Supplementary**
239 **Fig. 5**). The CD11b marker is required for monocyte migration to sites of inflammation[37], and is
240 highly expressed on myeloid cells recruited from the blood and differentiating into
241 macrophages[38]. We also observed an increase in the percentage of CD11b+ CD16+ HLA-DR+
242 CD206– myelomonocytic cells in BAL at week 2 and 3 following infection (**Fig. 2I**), a
243 population that is involved in regulating lung inflammatory response[20,33,39,40]. The gating strategy
244 for the two myelomonocytic cells populations is shown in **Supplementary Figure 4G**.
245
246 **Interstitial macrophages accumulate in lungs of infected animals.** Lungs were collected for
247 all animals at the end of the study, corresponding to 4 weeks post infection (1 week following the
248 last BAL collection shown in Figure 2), with the exception of NC33 and NC34. These two
249 animals had higher levels of IL-6 at necropsy compared to the other six monkeys, and NC34 had
250 symptoms similar to ARDS[18] (**Fig. 3**). Overall, infiltration of macrophages was observed in the
251 lungs of SARS-CoV-2 infected AGM and RM at necropsy and was more robust in animals with
252 severe disease (**Fig. 3A**). We further characterized macrophages population in the lung by
253 staining with the AM marker CD206 (in blue) and with CD11b integrin (in green) and CD16
254 (red) (**Fig. 3B**). Low numbers of macrophages were seen in the lungs of a non-infected control
255 RM, scattered throughout the interstitium and alveolar spaces, as shown by the arrows. In the
256 control this population was bi-morphic and composed of CD11b negative CD16+ CD206–
257 (arrow) in the alveolar septa or CD16+ CD206+ cells within the alveolar spaces (arrowhead)
258 (**Fig. 3B**). In all animals that were infected we could detect CD11b+ CD16+ macrophages. FR04

259 (RM ranking = 7) lungs had macrophages scattered throughout the interstitium and alveolar
260 spaces. The phenotypic population was heterogeneous and contained low numbers of CD11b+
261 CD16+ CD206– macrophages. The most severe RM, GH99 (ranking = 3), had large numbers of
262 macrophages multifocally surrounding small airways denoted by the asterisks. Of note this
263 animal had the higher absolute number of monocytes in the blood at week 1 (**Supplementary**
264 **Fig. 1D**). Low numbers of CD11b+ CD16+ CD206– cells were scattered throughout the
265 predominant population of CD11b+ CD16+ CD206+ macrophages. Macrophages were also
266 scattered throughout the interstitium and alveolar spaces. NC34 and NC33 (AGM ranking = 1
267 and 2 respectively) had multifocal to coalescing areas of hemorrhage (NC33 indicated by the
268 arrows), and pulmonary parenchyma infiltrated by multifocal aggregates of macrophages (NC34)
269 with infiltration by low to moderate numbers of macrophages. The phenotypic population was
270 heterogenous and composed of moderate numbers of CD11b+ CD16+ CD206– macrophages.
271 Aggregates were determined by staining animals FR04, GH99, and NC34 with CD68/CD163
272 (red) and CD3: (blue). Animal FR04 (RM ranking = 7) had isolated CD3+ cells scattered
273 throughout the lung. GH99 (RM ranking = 3) had cell aggregate with mixed populations of
274 CD3+ and CD68/CD163+ cells in isolated area of inflammation. NC34 (AGM ranking = 1) had
275 rare, small aggregates of CD3+ cells (**Supplementary Figure 6**). Altogether these findings
276 present a picture of long-lasting lung inflammation that, albeit more pronounced in animals with
277 severe signs of disease, is also present in animals with no detectable viral load and mild or no
278 signs of disease after 4 weeks from the start of infection.
279
280 **Neutrophils accumulate in animals with severe disease.** In this study we did not observe
281 changes in the absolute number of neutrophils in blood during the course of the infection

282 (**Supplementary Figure 1H**). Interestingly, studies in monkeys and humans showed increased
283 levels of neutrophils and suggested deregulation of their maturation, with CD11b being one of
284 the markers defining pre-neutrophils[8,9,41-43]. We stained lungs from animals NC33, NC34, GH99,
285 FR04 and NC40 with anti-myeloperoxidase (MPO) antibody for neutrophils and with anti-
286 CD11b antibody, and we included two controls, one RM and one AGM (**Figure 4A**). MPO+
287 cells[44] were elevated in animals with severe disease (NC33, NC34). GH99 had areas with
288 neutrophil accumulation and the remaining animals were low. Controls had very few neutrophils
289 in the lungs (**Figure 4B**). CD11b+ MPO+ neutrophils were only present in infected animals and
290 were also high in NC33 (**Figure 4C**). Accordingly, neutrophils and lymphocytes could be seen in
291 animals with severe disease but not in animals with moderate disease (**Supplementary Fig. 7**).
292 NC34 (necropsy day 8 post infection; rank = 1, severe) had lymphocytic aggregates that were
293 perivascular and intermixed with neutrophils and histiocytes. In NC38 (necropsy day 28, rank 5,
294 moderate) lymphocytic aggregates are scattered within the alveolar septa and predominately
295 mixed with histiocytes and rare neutrophils.
296
297 **NKG2a+ cells and PD-1+ T cells decrease in blood and increase in BAL overtime.**
298 Infiltration of lymphocytes was observed in the lungs of SARS-CoV-2 infected AGM and RM at
299 necropsy and was more robust in animals with severe disease (**Fig. 5A**). We first analyzed the
300 kinetics of innate NK cells subsets, that we defined as HLA-DR– CD3– cells expressing the
301 NKG2a receptors, which are known to traffic to the lung[45] (**Fig. 5B - D**, and **Supplementary**
302 **Fig. 8**). Interestingly, the frequencies of NKG2a+ cells significantly decreased in peripheral
303 blood of both AGM and RM over the course of infection (baseline vs. week 3, P = 0.03) (**Fig.**
304 **5B**). Consistent with the pattern described for the myeloid population, we also observed a

305 concomitant increase in the frequencies of NKG2a+ cells in BAL (baseline vs. week 3, P = 0.05)
306 (**Fig. 5C** and **5D**, **Supplementary Fig. 8A - 8C**). Four out of four AGM had decreased NKG2a+
307 cells in peripheral blood, coinciding with an increase of the same cells in BAL. While the pattern
308 of NKG2a+ cells in peripheral blood of RM was not statistically significant, nonetheless in this
309 species there was a marked increase of those cells in the BAL. These results suggest that the loss
310 of NKG2a+ cells in the PBMCs and the gain of NKG2a+ cells in the BAL may coincide with an
311 egress of these cells from peripheral blood to tissues. Accordingly, the frequency of NKG2a+
312 cells expressing CXCR3, a marker associated with NK cell migration to the lung[46] also
313 significantly decreased in blood over time (baseline vs. week 3, P = 0.03, **Fig. 5E**). Despite this
314 change in lymphocyte phenotype, the absolute number of lymphocytes did not change over the
315 first 2 weeks of infection (**Fig. 5F**) however it is important to note that all 3 remaining AGM had
316 an increase at week 3 (**Supplementary Fig. 8D – 8E**).
317 tSNE analysis revealed an increase in the level of PD-1 at weeks 2 and 3 post-infection,
318 overlapping with spatial regions corresponding to both CD4+ T and CD8+ T cells (**Fig. 5G and**
319 **Supplementary Fig. 9A**). In fact, the frequency of PD-1+ CD4+ T cells was elevated in the
320 blood of both RM and AGM (**Fig. 5H**, and **5I**, respectively). During the first week following the
321 infection we observed an increase in IP-10 and IFN-γ (**Supplementary Fig. 9B**), however we
322 also observed a switch toward Th2 type responses characterized by the increase of Th2 cytokines
323 IL-5 and IL-13 over time (**Supplementary Fig. 9B**). Accordingly, a gradual increase of Th2 type
324 cells (defined as CXCR3– CCR6 – CD4+ T cells)[24] was seen in the blood within the PD-1
325 positive population (**Fig. 5J**). The increase of PD-1+ Th2 cells was significantly and positively
326 associated with IL-4 cytokine levels (P = 0.016, R = 0.94, Spearman test) (**Supplementary Fig.**
327 **9C**). Moreover, we observed an increased level of PD-1+ CD8+ T cells in blood and BAL (BAL:

328 baseline vs. week 2, P = 0.015; baseline vs. week 3, P = 0.03) (data not shown and **Fig. 5K**).
329 Animals divided by species are shown in **Supplementary Fig. 9D** and **9E**. Associations between
330 viral replication and the frequency of PD1+ CD4 T cells in blood and PD1+ CD8 T cells in BAL
331 at week 3 were found (**Supplementary Fig. 9G- I),** however, they were most likely driven by
332 the AGM but not RM which had no detectable viral replication in bronchial brushes at that
333 specific time point.
334
335 The ratio between the anti-inflammatory and proinflammatory responses is associated with
336 disease progression. The pro-inflammatory cytokine IL-6 has been described as a strong
337 predictor to disease progression in humans[3,7]. We measured IL-6 and IL-10 in the plasma of all
338 the animals (**Fig. 6A**). While IL-6 levels alone did not associate with disease severity in NHPs,
339 the ratio of IL-10 to IL-6 levels measured in plasma associated with both the ranking of disease
340 severity and with the pathological score that was obtained by analyzing the extension of the
341 inflammation and edema of the lungs (R = 0.76 P = 0.037; and R = –0.76, P = 0.03, by the
342 Spearman correlation test, all animals) (**Fig. 6B** and **C**). To investigate further, we also measured
343 the levels of tryptophan and kynurenine in plasma at baseline, week 1, week 3 and at necropsy
344 (**Supplementary Figure 10**). Kynurenine was elevated and significantly increased at week 3
345 compared to baseline levels (P= 0.013 adj.). The kynurenine (Kyn)/ tryptophan (Tryp) ratio has
346 been used as a measurement of the indoleamine 2,3-dioxygenase (IDO) activity and is often
347 associated with T regulatory cell function [(21)]. In line with the observed association for the IL-
348 10:IL-6 ratio, the Kyn /Tryp ratio was also negatively correlated with the pathology score (1 =
349 mild – 18 = severe) suggesting that animals with higher levels of immune suppression had less
350 inflammation in the lung and better disease outcome (**Figure 6D**).

351 These findings show a complex series of immune events in the lung of that are most likely
352 initiated as a host response to the virus and then evolving overtime toward less antiviral
353 responses, as summarized in **Figure 6E.**
354

355 **DISCUSSION**
356
357 There is an urgent need to develop safe and effective strategies to prevent and treat COVID-19.
358 The development of such strategies requires a clear understanding of the immune cells involved
359 in COVID-19 and their unique role in pathogenesis. Clinical observations in patients and few
360 studies on non-human primates have started to shed light on the immune aspects involved in
361 COVID-19[8,9,11,22,47,48]. Here, we further characterized immune events following SARS-CoV-2
362 infection in two NHPs models recapitulating crucial aspects of COVID-19 lung disease[16,18].
363

364 Altogether our findings provide the first evidence in both AGM and RM of a multiphasic
365 immune response characterized by 1) an initial inflammatory phase with monocyte recruitment
366 to the lung 2) a gradual switch from a type 1 to type 2 response, and 3) a "make it or break it"
367 phase with either an increase in anti-inflammatory cytokines IL-10 and regulatory cell subsets
368 with suppressive activity, or IL-6, a pro-inflammatory cytokine associated with disease
369 progression in humans, as summarized in **Figure 6E**.

370 By examining the temporal and spatial distribution of monocytes, myelomonocytic cells and
371 macrophages in blood and BAL and lungs, we confirmed and extended on studies in humans and
372 NHPs suggesting increased myelopoiesis with recruitment of myeloid cells from the blood to
373 lungs during the infection that is initially driven by the virus replicating in the lung[3,16,22]. Similar
374 to what has been described by Wilk *et al.* and Thevarajan *et al.* in humans, we observed an

375 increase of classical CD14hi monocytes, and a corresponding drop in the frequency of
376 monocytes expressing CD16 in the peripheral blood[22,23]**.** Importantly, we extend on these
377 findings by showing a simultaneous increase in the frequency patrolling CD16hi HLA-DR+
378 monocytes in BAL occurring in both species and by describing the kinetics of two CD16+ HLA-
379 DR+ CD206– macrophages populations that preferentially populate the alveolar interstitium and
380 exhibit features of antigen-presenting cells[49]. CD11c+ CD16+ cells arising from intravascular
381 CD16hi patrolling monocytes in the acute phase and associating with IL-6 levels, and a CD11b+
382 macrophage population known to be involved in resolution of inflammation in the lung[20,33,39,40].
383 Higher frequencies of CD11b+ monocytes with increased disease severity has been observed in
384 the blood of humans[8]. The origin and the exact function of these interstitial macrophages remains
385 to be determined.

386 Differently than what was observed in humans and previously reported data in RM, we did not
387 detect an increase in the number of neutrophils, as these responses may have come up earlier
388 than 1 week after infection as shown by others[16]. At necropsy, CD11b+ MPO+ neutrophils were
389 present in the lungs of animals with severe disease as observed in humans. More studies are
390 needed to determine if SARS-CoV-2 results in the accumulation of immature neutrophils as seen
391 in humans [8,9].
392
393 Common to both species was the observation that animals with higher levels of myeloid and
394 lymphoid cell infiltration in the lung had worse disease outcomes. Several studies in both SARS-
395 CoV-1 and CoV-2 have reported depleted peripheral NK cell counts in severe patients[11,22,25,47].
396 Our data support the notion of NKG2a+ cell trafficking to the lung during SARS-CoV-2
397 infection, most likely mediated by IP-10 (CXCL-10), which promotes the recruitment of

398 CXCR3+ Th1 thymocytes and NKs[50,51]. Expression of NKG2a has been linked to both activation
399 and inhibition of inflammation[52]; the function in SARS-CoV-2 remains to be investigated. In the
400 periphery, we also observed increased levels of PD-1 on T cells. This is consistent with findings
401 in humans describing of an exhaustive T cell phenotype during SARS-CoV-1 and CoV-2
402 infection[11,53].
403
404 For the first time, we identified TARC (CCL17) as a possible mediator of myeloid recruitment in
405 the lung during SARS-CoV-2. Both dendritic cells and CD11b+ macrophages in the lung have
406 been identified as a source of CCL17 in the airways in other pulmonary inflammatory
407 diseases[54,55].These cells promote the recruitment of T helper type 2 (Th2) lymphocytes into the
408 airways[54]. Remarkably, we observed a gradual increase of the recruitment of Th2 lymphocytes
409 into the airway and of Th2 type cytokines such as IL-5 and IL-13. These findings show a
410 complex series of immune events in the lung of that are most likely initiated as a host response to
411 the virus, and that they may evolve into other less effective antiviral responses as either an
412 attempt to tissue repair/resolution of inflammation, as summarized in **Figure 6E,** or as the result
413 of virus direct immunomodulatory effects on host responses[6].
414
415 Intrinsic species-specific susceptibility to disease progression has been described for NHP in
416 SARS-CoV-1[6] with AGM being more susceptible than rhesus to severe disease. There were
417 unexpected similarities in the kinetics and the quality of the immune responses analyzed in RM
418 and AGM, particularly during the acute phase of infection, however AGM did not clear the
419 infection as well as RM and two AGM had most severe symptoms[56]. While the number of
420 animals enrolled in this study was not sufficient to look at species-specific differences and their

421 effect on disease progression, we found that a higher ratio of IL-10: IL-6 in plasma was
422 associated with disease severity. Undoubtedly, more studies are needed to prove or disprove the
423 single contribution of IL-10 and IL-6 in the outcome of COVID-19 disease and to identify the
424 source of these two potential key players[57]. The notion that dynamically balanced pro and anti-
425 immune responses to SASR-CoV-2 play an important role in disease progression and outcome is
426 supported by the association of the pathological score and the Kyn /Tryp suggesting a role of T
427 regulatory cells in resolution of inflammation of the lungs in COVID-19.
428
429 Overall, this study uncovers critical steps in the immune events of the host response to SARS-
430 CoV-2 and describes new correlates of viral replication and disease progression. Importantly, we
431 show viral driven inflammation/cell recruitment to the lung occurs rapidly, and lasts up to four
432 weeks post infection, which may explain in part the observed slow recovery from COVID-19
433 seen humans. Finally, these findings have the potential to aid the interpretation of the results of
434 the human trials that are currently underway for several vaccine candidates and may be
435 instrumental in generating new targeted therapeutic strategies aimed at resolving the severe
436 immune deregulation of the lung of COVID-19 patients.
437

438 **Methods**
439
440 **Ethical statement on animal use and SARS-CoV-2 handling.** Animals and infection. The
441 Institutional Animal Care and Use Committee of Tulane University reviewed and approved all
442 the procedures for this study. The Tulane National Primate Research Center is fully accredited
443 by the AAALAC. All animals were cared for in accordance with the ILAR Guide for the Care
444 and Use of Laboratory Animals 8th Edition. The Tulane University Institutional Biosafety

445 Committee approved the procedures for sample handling, inactivation, and transfer from BSL3
446 containment.
447
448 **Animals and infection**. Four adult-aged African green monkeys (Caribbean origin) and four
449 rhesus macaques (Indian ancestry) were exposed to SARS-CoV-2; 2019-nCoV/USA-WA1/2020
450 409 (MN985325.1). The virus stock was prepared in Vero E6 cells and the sequence confirmed
451 by PCR and/or Sanger sequencing. Plaque assays were performed in Vero E6 cells. The rhesus
452 macaques were from the Tulane National Primate Research Center breeding colony pathogen
453 free for simian type D retrovirus (SRV), macacine herpesvirus 1 (B virus), simian
454 immunodeficiency virus (SIV), simian T cell lymphotropic/leukemia virus (STLV), measles
455 virus (MV) and tuberculosis (TB). The African green monkeys were wild caught and at the
456 TNPRC for over a year before being assigned to this study. To mimic different possible routes of
457 infection in humans, animals were exposed to the virus either by aerosol (inhaled dose of 2.0 x
458 10^3 and 2.5 x 10^3 $TCID_{50}$) or by inoculating a cumulative dose of 3.61 x 10^6 PFU through
459 multiple routes (oral, nasal, intratracheal, conjunctival) (**Supplementary Table 1**).
460 The multi route exposure was given to four animals, one adult RM male (GH99, 14 years old),
461 one adult RM female (HD09, 13 years old) and two AGM, one aged male (NC40, 16 years old,
462 approximately) and one aged female (NC33, 16 years old, approximately). An additional two
463 adult males RM (FR04 and HB37, 15 and 13 years old, respectively) and one aged male and
464 female AGM: NC34 and NC38 (16 years old, approximately) were exposed by aerosol
465 (**Supplementary Table 1**). Rhesus macaques tend to live approximately 20 years in captivity,
466 while African green monkeys live approximately 15 years[58]. The age of the macaques is
467 generally multiplied by three when compared to humans, and GH99 had signs of aged lungs that
468 were not associated with COVID-19.

469
470 **Cell count and CO_2 and SpO_2 pressure measurements.** Total white blood cell counts, white
471 blood cell differentials, red blood cell counts, platelet counts, hematocrit values, total
472 hemoglobin concentrations, mean cell volumes, mean corpuscular volumes, and mean
473 corpuscular hemoglobin concentrations were analyzed from blood collected in tubes containing
474 EDTA using a SYSMEX XN-1000v Hematology Analyzer in the Level 2 Lab and a Sysmex XS-
475 1000 in the Level 3 Lab. CO_2 measurements were taken using the Piccolo Express Chemistry
476 Analyzer in the Level 3 lab and is part of the Metabolic Comprehensive Panel. SpO_2 values were
477 obtained using the Masimo Rad-57 Handheld Pulse Oximeter (**Supplementary Table 3**).
478
479 **Sample collection and processing.** Blood EDTA was collected by venipuncture and bronchial
480 brush and BAL by bronchoscopy. For the latter, the bronchoscope is introduced into the trachea
481 and directed into one of the bronchi. The bronchoscope is advanced to the point where the
482 diameter of the bronchoscope approximates the dimensions of the bronchus. The bronchial brush
483 is passed through the channel of the bronchoscope. The brush is gently advanced until the lumen
484 of the bronchus or bronchioles approximates the dimensions of the brush. The brush is then be
485 gently advanced back and forth against the mucosa to gather cells. The brush is removed from
486 the channel of the bronchoscope and the brush is placed into 200 µL of DNA/RNA Shield X1
487 (Cat.# R1200, Zymo Research, Irvine, CA). The bronchoscope remains in place while two
488 aliquots of 20 ml of saline each are instilled into the bronchus and subsequently aspirated. This
489 procedure is then repeated in the opposite lung.
490
491 Blood was layered over Ficoll-Plaque Plus (GE Healthcare17144003) and centrifuged for 30
492 minutes in cap-locked adaptors. Differential migration of cells during centrifugation results in

493 the formation of layers containing different cell types and allows collection of peripheral blood
494 mononuclear cells (PBMCs) from other populations. PBMCs were collected, counted and
495 aliquoted in tubes or resuspended in freezing media containing Fetal Bovine Serum and DMSO.
496 For bronchoalveolar lavage (BAL), cells and supernatant were separated by centrifugation (15
497 minutes at 2,000 x g at RT) in cap-locked adaptors and cells were lysed in Ammonium Chloride
498 Potassium (ACK) lysing buffer at room temperature for 5 minutes (Gibco# A1049201) washed
499 in 2% FBS, and resuspended in PBS and counted under laminar flux hood in BCL3. Fresh cells
500 were stained for flow cytometry.
501
502 **BAL and PBMCs staining.** Freshly obtained PBMCs and cells obtained from BAL were stained
503 with appropriate antibody cocktails and incubated for 30 minutes at room temperature.
504 Antibodies are listed in **Supplementary Table 10.** Cells were fixed with 4% or 2% PFA-BSA
505 overnight. Samples were run on a FACSAria Fusion flow cytometer (Becton Dickinson) within a
506 Biosafety Cabinet, and each sample was run for at least five minutes. For all panels, the
507 LIVE/DEAD Fixable Aqua Dead cell Stain kit was used (ThermoFisher #L34957). Monocytes
508 subsets were gated as described in **Supplementary Figure 2A** and as previously described[24].
509 Alveolar macrophages were gated based on the size and the expression of HLA-DR, CD206 and
510 CD163 markers. Myeloid infiltrates were gated as cells negative for CD206 and CD163 and
511 positive for HLA-DR, CD16 and CD11b. The gating strategy is shown in **Supplementary**
512 **Figure 4G**. NKG2a+ cells were gated on the CD3 negative parent population as shown (BAL
513 FR04 week 2) in **Supplementary Figure 8A.** Th1, Th2, and Th17 cells were gated as previously
514 described[24]. tSNE analyses were performed in FlowJo using the opt-SNE algorithm and plots
515 were created in R using the ggplot2 package[59].
516

517 **Histopathology and scoring.** Tissue samples were fixed in Z-fix (Anatech), embedded in
518 paraffin and 5 μm thick sections were cut, adhered to charged glass slides and stained with
519 hematoxylin and eosin. All slides were scanned on a Zeiss Axio Scan.Z1 digital slide scanner.
520 Images were acquired using HALO software (Indica Labs). Quantification of pathologic lesions
521 was performed with HALO software. Machine learning (Random Forest) algorithms were
522 trained by a board -certified pathologist to recognize fluidic and cellular inflammation in the
523 lungs of the RM and AGM. Scores were assigned to fluidic and cellular inflammation,
524 separately, based on the percentage of lung affected. Fluidic and cellular inflammation scores
525 were summated for all lobes and animals were ranked from 1 (highest sum) to 8 (lowest sum).
526
527 **Plasma cytokines and chemokines.** Plasma was collected by spinning and was thawed before
528 use. Cytokines were measured using 497 Mesoscale Discovery. IFN-γ, IL-4, IL-6, IL-8, IL-10
529 and IL-13 were part of the V-Plex Proinflammatory Panel 1, 10-Plex. V-plex. The chemokine
530 panel (#K15049D, Mesoscale Discovery, Rockville, Maryland) was also used, following the
531 instructions of the kit. The plate was read on a MESO Quickplex 500 SQ120 machine.]
532 Heatmaps were generated using the 'pheatmap' package in R[60,61]. Data were normalized by
533 dividing raw values at week 1 by baseline values for each animal, followed by the application of
534 $\log_2$. Values below the limit of detection were replaced with the lowest limit of detection value
535 based on the standard curve for each run, or with the lowest value detected during the run,
536 whichever was smaller. Bubble plots were generated using the 'ggplot2' package in R, using the
537 same normalized data shown in the heatmap[59]. Scatter plots were drawn using raw data points
538 and display Pearson's correlation coefficients and a 95% confidence interval.
539

540 **RNA isolation**. Swab and bronchial brush samples were collected in 200 µL of
541 DNA/RNA Shield X1 (Cat.# R1200, Zymo Research, Irvine, CA) and extracted for Viral RNA
542 (vRNA) using the Quick-RNAViral kit (Cat.# R1034/5, Zymo Research). The Viral RNA
543 Buffer dispensed directly to the swab in the DNA/RNA Shield. The swab was directly inserted
544 into the spin column. The vRNA was eluted (45µL) and 5 µL was added in a 0.1 mL fast 96-well
545 optical microtiter plate (Cat.# 4346906, ThermoFisher, CA).
546
547 **Viral RNA detection.** RT-qPCR reaction TaqPath1-Step MultiplexMaster Mix was used (Cat.#
548 A28527, ThermoFisher) along with the 2019-nCoV RUO Kit (Cat.# 10006713, IDTDNA,
549 Coralville, IA) targeting the N1 amplicon of N gene of SARS2-nCoV19 (accession MN908947).
550 The master mix was added to the microtiter plates covered with optical film (cat. #4311971;
551 ThermoFisher) and then was vortexed and pulse centrifuged. The RT-qPCR program consisted
552 of incubation at 25°C for 2 minutes, RT incubation at 50°C for 15 minutes, and an enzyme
553 activation at 95°C for 2 minutes followed by 40 cycles of denaturing step at 95°C for 3 seconds
554 and annealing at 60°C for 30 seconds. Fluorescence signals were detected with an Applied
555 Biosystems QuantStudio6 Sequence Detector. Data were captured and analyzed with Sequence
556 Detector Software v1.3 (Applied Biosystems, Foster City, CA). Viral copy numbers were
557 calculated by plotting Cq Values obtained from unknown (i.e. test) samples against a standard
558 curve representing known viral copy numbers. The limit of detection of the assay was 10 copies
559 per reaction volume. A 2019-nCoVpositive control (Cat.#10006625, IDTDNA) were analyzed in
560 parallel with every set of test samples. A non-template control (NTC) was also included.
561
562 **Immunohistochemistry.** Five µm sections of Formalin-fixed, paraffin-embedded lung were
563 mounted on charged glass slides, baked overnight at 56ºC and passed through Xylene, graded

564 ethanol, and double distilled water to remove paraffin and rehydrate tissue sections. A
565 microwave was used for heat induced epitope retrieval, which was performed sequentially with
566 high and low pH solutions from Vector Labs (H-3301 and H-3300). CD16+ and MPO+ cells
567 were detected using MACH3 AP kits (Biocare Medical M3M532 or M3R533) and permanent
568 red substrate (Dako K0640). MPO+ cells CD3+ cells CD11b+ cells CD68+/CD163+ cells, and
569 CD206+ cells were detected using antibodies described in **Supplementary Table 10**. Slides
570 were incubated with a blocking buffer comprised of either 1% normal donkey serum or 10%
571 normal goat serum for 40 minutes. All primary antibodies were incubated for 60 minutes and all
572 secondary antibodies for 40 minutes at room temperature, with thorough washing in between.
573 DAPI (4',6-diamidino-2-phenylindole) was used to label the nuclei of each section. Slides were
574 mounted using a homemade anti-quenching mounting media containing Mowiol (Calbiochem
575 #475904) and DABCO (Sigma #D2522) and imaged with a Zeiss Axio Slide Scanner.
576
577 **Arginase Activity.** Arginase activity was analyzed on Plasma using the Arginase Activity Assay
578 Kit (MAK112, Sigma-Aldrich, St. Louis, MO) following the manufacturer instructions. Briefly,
579 samples were thawed on ice and, in order to deplete the urea, 40 µl of plasma were loaded in an
580 Amicon®Ultra 10K centrifugal filter (UFC501096 EMD Millipore), diluted with pure water to
581 500 µl, and centrifuged at 13,000 × g for 30 min at 4°C. Following centrifugation, the eluted
582 solution was discarded. Filtered samples were then diluted with pure water to 500 µl, and
583 centrifuged at 13,000 × g for 30 min at 4°C. At the end of centrifugation, the remaining volume
584 of each sample was measured, and ultra-pure water was added to reach a final volume of 40 µl.
585 Each sample was loaded into 2 wells of a 96-well plate (20 µl/well), representing the sample well
586 and the sample blank well, and 20 µl/well of ultra-pure water were added to each well. Together

587 with samples, the plate was loaded with urea standard and water as positive and negative
588 controls, respectively. Samples were loaded in singlicate, whereas controls were loaded in
589 duplicate. Ten microliters of 5X substrate buffer, composed of Arginine Buffer and Mn Solution,
590 were added to the wells except for sample blank wells, and they were incubated for 120 min at
591 37°C. Following the incubation, 200 µl of Urea Reagent, composed of Reagents A and B, was
592 added to each well to stop the reaction. Finally, 10 µl of 5X Substrate Buffer was added to the
593 sample blank wells to have the same reagents proportion of reagents as the Sample Wells. After
594 mixing, the plate was incubated for 60 min at RT, and finally acquired with microplate
595 spectrophotometer Power Wave XS2 (BioTek Instruments, Winooski, VT) to measure the
596 absorbance at 430 nm (A_{430}) of each well. The arginase activity was determined per the
597 following equation: [(sample well) - (blank)/(urea- blank)] X [(1mM x50x 103)/40ul x
598 120min)], according to the manufacture instructions.
599
600 **Kynurenine and Tryptophan Plasma Levels.** Tryptophan and Kynurenine plasma
601 concentrations were measured by using the Tryptophan ELISA (Rocky Mountain Diagnostics,
602 Colorado Springs, CO, USA, Catalog #BA E-2700) and Kynurenine ELISA commercial kits
603 (Rocky Mountain Diagnostics, Colorado Springs, CO, USA, Catalog #BA E-2200). For
604 tryptophan measurement, 20 µl of plasma were precipitated, the recovered supernatants were
605 derivatized, and the product was used to perform the ELISA according to manufacturer
606 instructions. For kynurenine assay, 10 µl of plasma were acylated and used to perform the
607 ELISA according to manufacturer instructions. The data are presented as the ratio between
608 kynurenine and tryptophan (Krn/Try) levels.
609

610 **Statistical analysis.** Correlation analyses were performed using the non-parametric Spearman
611 rank correlation method (two-tailed, 95% confidence) using exact permutation P values when
612 ranks were used, or Peason's correlation test when both variables were continuous. Analysis of
613 variance (ANOVA) was used for comparing statistical differences between multiple groups,
614 followed by Dunn's multiple comparison tests. Kruskal-Wallis ANOVA or Mann-Whitney tests
615 were used. All statistical analyses were performed using GraphPad Prism (version 8.4.2
616 GraphPad Software, La Jolla California USA) and R software (URL http://www.R-project.org/).
617 Correlation plots were created using the 'Performance Analytics' and 'corrr' plots, respectively,
618 in R[61-63].
619
620

621 **Acknowledgments**

622 We would like to thank Dr. Joseph (JC) Mudd and Dr. Cariappa Annaiah for critical reading of
623 the manuscript and Dr. Amitinder (Miti) Kaur, Megan Varnado, Kaitlin Didier from the TNPRC
624 Flow Cytometry Core for their help. We thank Angela Birnbaum for reviewing and optimizing
625 all technical SOPs and overseeing the safety of this study.
626 We would also like to thank Fast Grant Funding for COVID-19 Science for partially funding this
627 work and the NIH for supporting this work through the TNPRC base grant (P51 OD011104 59).
628

629 **Competing Interests statement**
630 **All data will be made available upon acceptance.**

631 These authors declare no competing interests.

632
633 **Author Contributions**
634 MDF analyzed data composed figures and wrote the manuscript, BRV was the lead pathologist and
635 LADM was the project veterinarian, contributed to study design, and writing of the IACUC and
636 manuscript. CCM designed IHC panels and performed the IHC staining, GZ wrote the manuscript, KERL
637 was a project veterinarian, made clinical assessments and collected samples, CJM processed and analyzed
638 samples for RT-qPCR, contributed; EHH provided the mesoscale data, TPP stained the samples with GL
639 and BMT. GL contributed to study design, provided administrative support, and aided with sample
640 processing and archiving. NG contributed to study design, study coordination, sample processing, and
641 SOP development. PKD processed and analyzed viral load data. CJR conceived and performed aerosol

experiments. RPB contributed to study design, analysis of clinical and imaging results, and writing the manuscripts. NJM performed staining of BAL and contributed to writing the manuscript. TF contributed to the animal study design and planning and contributed to writing the manuscript. JR designed and supported the animal study and helped with the writing of the manuscript. MV conceived and supported the study, run experiments, analyzed data and wrote the manuscript.

REFERENCES

1. Guan, W.J., *et al.* Clinical Characteristics of Coronavirus Disease 2019 in China. *N Engl J Med* **382**, 1708-1720 (2020).
2. Sun, P., *et al.* Clinical characteristics of hospitalized patients with SARS-CoV-2 infection: A single arm meta-analysis. *J Med Virol* **92**, 612-617 (2020).
3. Blanco-Melo, D., *et al.* Imbalanced Host Response to SARS-CoV-2 Drives Development of COVID-19. *Cell* **181**, 1036-1045.e1039 (2020).
4. Weiss, S.R. Forty years with coronaviruses. *J Exp Med* **217**(2020).
5. Clay, C., *et al.* Primary severe acute respiratory syndrome coronavirus infection limits replication but not lung inflammation upon homologous rechallenge. *J Virol* **86**, 4234-4244 (2012).
6. Graham, R.L., Donaldson, E.F. & Baric, R.S. A decade after SARS: strategies for controlling emerging coronaviruses. *Nat Rev Microbiol* **11**, 836-848 (2013).
7. Ruan, Q., Yang, K., Wang, W., Jiang, L. & Song, J. Clinical predictors of mortality due to COVID-19 based on an analysis of data of 150 patients from Wuhan, China. *Intensive Care Med* **46**, 846-848 (2020).
8. Silvin, A., *et al.* Elevated Calprotectin and Abnormal Myeloid Cell Subsets Discriminate Severe from Mild COVID-19. *Cell* (2020).
9. Schulte-Schrepping, J., *et al.* Severe COVID-19 Is Marked by a Dysregulated Myeloid Cell Compartment. *Cell* (2020).
10. Xiong, Y., *et al.* Transcriptomic characteristics of bronchoalveolar lavage fluid and peripheral blood mononuclear cells in COVID-19 patients. *Emerg Microbes Infect* **9**, 761-770 (2020).
11. Zhou, Y., *et al.* Pathogenic T cells and inflammatory monocytes incite inflammatory storm in severe COVID-19 patients. *National Science Review* (2020).
12. Crooke, S.N., Ovsyannikova, I.G., Poland, G.A. & Kennedy, R.B. Immunosenescence and human vaccine immune responses. *Immun Ageing* **16**, 25 (2019).
13. Gretebeck, L.M. & Subbarao, K. Animal models for SARS and MERS coronaviruses. *Curr Opin Virol* **13**, 123-129 (2015).
14. McAuliffe, J., *et al.* Replication of SARS coronavirus administered into the respiratory tract of African Green, rhesus and cynomolgus monkeys. *Virology* **330**, 8-15 (2004).
15. Chandrashekar, A., *et al.* SARS-CoV-2 infection protects against rechallenge in rhesus macaques. *Science* (2020).
16. Singh, D.K., *et al.* SARS-CoV-2 infection leads to acute infection with dynamic cellular and inflammatory flux in the lung that varies across nonhuman primate species. *BioRxiv* (2020).
17. Yu, J., *et al.* DNA vaccine protection against SARS-CoV-2 in rhesus macaques. *Science* (2020).

688 18. Blair, R.V., *et al.* ARDS and Cytokine Storm in SARS-CoV-2 Infected Caribbean
689 Vervets. *BioRxiv* (2020).
690 19. Munster, V.J., *et al.* Respiratory disease in rhesus macaques inoculated with SARS-CoV-
691 2. *Nature* (2020).
692 20. Aggarwal, N.R., King, L.S. & D'Alessio, F.R. Diverse macrophage populations mediate
693 acute lung inflammation and resolution. *Am J Physiol Lung Cell Mol Physiol* **306**, L709-
694 725 (2014).
695 21. Fallarino, F., *et al.* The combined effects of tryptophan starvation and tryptophan
696 catabolites down-regulate T cell receptor zeta-chain and induce a regulatory phenotype in
697 naive T cells. *J Immunol* **176**, 6752-6761 (2006).
698 22. Wilk, A.J., *et al.* A single-cell atlas of the peripheral immune response in patients with
699 severe COVID-19. *Nat Med* (2020).
700 23. Thevarajan, I., *et al.* Breadth of concomitant immune responses prior to patient recovery:
701 a case report of non-severe COVID-19. *Nat Med* **26**, 453-455 (2020).
702 24. Vaccari, M., *et al.* HIV vaccine candidate activation of hypoxia and the inflammasome in
703 CD14. *Nat Med* **24**, 847-856 (2018).
704 25. Wen, W., *et al.* Immune cell profiling of COVID-19 patients in the recovery stage by
705 single-cell sequencing. *Cell Discov* **6**, 31 (2020).
706 26. Vaccari, M., *et al.* Myeloid Cell Crosstalk Regulates the Efficacy of the
707 DNA/ALVAC/gp120 HIV Vaccine Candidate. *Front Immunol* **10**, 1072 (2019).
708 27. Lin, A., *et al.* Rhesus Macaque Myeloid-Derived Suppressor Cells Demonstrate T Cell
709 Inhibitory Functions and Are Transiently Increased after Vaccination. *J Immunol* **200**,
710 286-294 (2018).
711 28. Bronte, V., Serafini, P., Mazzoni, A., Segal, D.M. & Zanovello, P. L-arginine metabolism
712 in myeloid cells controls T-lymphocyte functions. *Trends Immunol* **24**, 302-306 (2003).
713 29. Anderson, C.A., *et al.* A degradatory fate for CCR4 suggests a primary role in Th2
714 inflammation. *J Leukoc Biol* **107**, 455-466 (2020).
715 30. Yang, Y., *et al.* Plasma IP-10 and MCP-3 levels are highly associated with disease
716 severity and predict the progression of COVID-19. *J Allergy Clin Immunol* (2020).
717 31. Pence, B.D. Severe COVID-19 and aging: are monocytes the key? *Geroscience* (2020).
718 32. Cai, Y., *et al.* In vivo characterization of alveolar and interstitial lung macrophages in
719 rhesus macaques: implications for understanding lung disease in humans. *J Immunol* **192**,
720 2821-2829 (2014).
721 33. Johnston, L.K., Rims, C.R., Gill, S.E., McGuire, J.K. & Manicone, A.M. Pulmonary
722 macrophage subpopulations in the induction and resolution of acute lung injury. *Am J*
723 *Respir Cell Mol Biol* **47**, 417-426 (2012).
724 34. Irjala, H., *et al.* Mannose receptor is a novel ligand for L-selectin and mediates
725 lymphocyte binding to lymphatic endothelium. *J Exp Med* **194**, 1033-1042 (2001).
726 35. Auffray, C., *et al.* Monitoring of blood vessels and tissues by a population of monocytes
727 with patrolling behavior. *Science* **317**, 666-670 (2007).
728 36. Landsman, L., *et al.* CX3CR1 is required for monocyte homeostasis and atherogenesis by
729 promoting cell survival. *Blood* **113**, 963-972 (2009).
730 37. Prieto, J., Eklund, A. & Patarroyo, M. Regulated expression of integrins and other
731 adhesion molecules during differentiation of monocytes into macrophages. *Cell Immunol*
732 **156**, 191-211 (1994).

733 38. Tam, J.W., Kullas, A.L., Mena, P., Bliska, J.B. & van der Velden, A.W. CD11b+ Ly6Chi
734 Ly6G- immature myeloid cells recruited in response to Salmonella enterica serovar
735 Typhimurium infection exhibit protective and immunosuppressive properties. *Infect*
736 *Immun* **82**, 2606-2614 (2014).
737 39. Liao, M.*, et al.* Single-cell landscape of bronchoalveolar immune cells in patients with
738 COVID-19. *Nat Med* **26**, 842-844 (2020).
739 40. Steinmüller, C., Franke-Ullmann, G., Lohmann-Matthes, M.L. & Emmendörffer, A.
740 Local activation of nonspecific defense against a respiratory model infection by
741 application of interferon-gamma: comparison between rat alveolar and interstitial lung
742 macrophages. *Am J Respir Cell Mol Biol* **22**, 481-490 (2000).
743 41. Scapini, P., Marini, O., Tecchio, C. & Cassatella, M.A. Human neutrophils in the saga of
744 cellular heterogeneity: insights and open questions. *Immunol Rev* **273**, 48-60 (2016).
745 42. Kwok, I.*, et al.* Combinatorial Single-Cell Analyses of Granulocyte-Monocyte Progenitor
746 Heterogeneity Reveals an Early Uni-potent Neutrophil Progenitor. *Immunity* **53**, 303-
747 318.e305 (2020).
748 43. Ng, L.G., Ostuni, R. & Hidalgo, A. Heterogeneity of neutrophils. *Nat Rev Immunol* **19**,
749 255-265 (2019).
750 44. Reumaux, D., de Boer, M., Meijer, A.B., Duthilleul, P. & Roos, D. Expression of
751 myeloperoxidase (MPO) by neutrophils is necessary for their activation by anti-
752 neutrophil cytoplasm autoantibodies (ANCA) against MPO. *J Leukoc Biol* **73**, 841-849
753 (2003).
754 45. Cong, J. & Wei, H. Natural Killer Cells in the Lungs. *Front Immunol* **10**, 1416 (2019).
755 46. Carlin, L.E., Hemann, E.A., Zacharias, Z.R., Heusel, J.W. & Legge, K.L. Natural Killer
756 Cell Recruitment to the Lung During Influenza A Virus Infection Is Dependent on
757 CXCR3, CCR5, and Virus Exposure Dose. *Front Immunol* **9**, 781 (2018).
758 47. National Research Project for SARS, B.G. The involvement of natural killer cells in the
759 pathogenesis of severe acute respiratory syndrome. *Am J Clin Pathol* **121**, 507-511
760 (2004).
761 48. Kuri-Cervantes, L.*, et al.* Immunologic perturbations in severe COVID-19/SARS-CoV-2
762 infection. *bioRxiv* (2020).
763 49. Schyns, J.*, et al.* Non-classical tissue monocytes and two functionally distinct populations
764 of interstitial macrophages populate the mouse lung. *Nat Commun* **10**, 3964 (2019).
765 50. Jiang, D.*, et al.* Regulation of pulmonary fibrosis by chemokine receptor CXCR3. *J Clin*
766 *Invest* **114**, 291-299 (2004).
767 51. Agostini, C.*, et al.* Cxcr3 and its ligand CXCL10 are expressed by inflammatory cells
768 infiltrating lung allografts and mediate chemotaxis of T cells at sites of rejection. *Am J*
769 *Pathol* **158**, 1703-1711 (2001).
770 52. Creelan, B.C. & Antonia, S.J. The NKG2A immune checkpoint - a new direction in
771 cancer immunotherapy. *Nat Rev Clin Oncol* **16**, 277-278 (2019).
772 53. Li, C.K.*, et al.* T cell responses to whole SARS coronavirus in humans. *J Immunol* **181**,
773 5490-5500 (2008).
774 54. Medoff, B.D.*, et al.* CD11b+ myeloid cells are the key mediators of Th2 cell homing into
775 the airway in allergic inflammation. *J Immunol* **182**, 623-635 (2009).
776 55. Alferink, J.*, et al.* Compartmentalized production of CCL17 in vivo: strong inducibility in
777 peripheral dendritic cells contrasts selective absence from the spleen. *J Exp Med* **197**,
778 585-599 (2003).

56. Woolsey, C., *et al.* Establishment of an African green monkey model for COVID-19. *bioRxiv* (2020).
57. Han, H., *et al.* Profiling serum cytokines in COVID-19 patients reveals IL-6 and IL-10 are disease severity predictors. *Emerg Microbes Infect* **9**, 1123-1130 (2020).
58. Simmons, H.A. Age-Associated Pathology in Rhesus Macaques (Macaca mulatta). *Vet Pathol* **53**, 399-416 (2016).
59. Wickham, H. ggplot2: Elegant Graphics for Data Analysis. (Springer-Verlag, New York, 2016).
60. Kolde, R. pheatmap: Pretty Heatmaps (2018).
61. Team, R.C. R: A language and environment for statistical computing. . (Foundation for Statistical Computing, Vienna, Austria, 2019).
62. Peterson, B.G. & Carl, P. PerformanceAnalytics: Econometric Tools for Performance and Risk Analysis. . (2020).
63. Kuhn, M., Jackson, S. & Cimentada, J. corrr: Correlations in R. (2020).

Figure Legend

Figure 1. Monocytes are a correlate of bronchoalveolar viral replication. (**A**) Schematic of study design. Arrows represent time of inoculation with SARS-CoV-2 (day 0) or sacrifice (up to 28 days post infection). Unless stated otherwise, rhesus macaque data are shown in teal, and African green monkey data are shown in magenta. (**B**) SARS-CoV-2 RNA levels in bronchial brushes over time. (**C**) Association between SARS-CoV-2 load in bronchial brushes and ranking of disease severity in all eight animals (most severe case = 1; mildest case = 8). (**D**) Changes in monocyte count in blood before and after infection. (**E**) Proportion of total monocytes (HLA-DR+ CD16+ and/or CD14+ out of CD45+ leukocytes) in PBMCs over time (baseline and week 1= 8 animals, week 2,3 = 7 animals). (**F**) Correlation between SARS-CoV-2 viral load in bronchial brushes and absolute count of monocytes in blood at one-week post-infection (1wk pi) (n= 8). (**G**) Representative flow cytometry changes in non-classical monocytes after the infection in blood (1wk pi). (**H**) Percent of classical (CD14hi CD16low) and (**I**) non classical monocytes (CD14low CD16hi) out of total monocytes in PBMCs (baseline = 8 animals week 1 = 4 animals, week 2, 3= 7 animals). (**J**) Correlation between monocytes absolute numbers in blood

811 and TARC (CCL17) in plasma (1wk pi). (**K**) Relationship between fold change of chemokines
812 and SARS-CoV-2 viral load in bronchoalveolar brushes (1wk pi). (**L**) Heatmap displaying log2
813 fold-change of 8 chemokines involved with traffic of monocytes to the lung. (1wk pi). Animals
814 are ordered by ranking of disease severity.
815
816 **Figure 2. Myelomonocytic cells increase in BAL is associated with IL-6.** (**A**) Decrease of
817 alveolar macrophages (HLA-DR+ CD206+ CD163+ cells) in the BAL after infection. (**B**)
818 Increase in the frequency of myelomonocytic infiltrates (HLA-DR+ CD206– CD163–) and (**C**)
819 of endothelial cells (HLA-DR+ CD206– CD163+) at infection in BAL (1wk pi). (**D**) tSNE plots
820 displaying kinetics of expression of CD16, CD11b and CD11c markers on live/ HLA-DR+ cells
821 populations in BAL before and after infection. (**E**) Gating of CD11c+ and CD11b+ populations
822 on the tSNE map based on antigen expression and discrete density clustering. (**F**)
823 Characterization of populations shown in (**E**). The heatmap depicts fold-change values of each
824 antigen compared to channel values of negative-expressing cell populations. (**G**) Increase in the
825 percentage of CD16+ HLA-DR+ cells and (**H**) in the percentage of interstitial macrophages
826 (CD16+ CD206– HLA-DR+) expressing of CD11c and (**I**) CD11b in BAL overtime.
827
828 **Figure 3. Interstitial macrophages are increased in the lung of SARS-CoV-2 infected**
829 **animals.** (**A**) Macrophage infiltration varied from minimal to severe in both rhesus and AGM
830 infected with SARS-CoV-2. (**B**) Fluorescent immunohistochemistry in the lung of AGM and
831 RM showing infiltration of CD16+ CD11b+ CD206– macrophages (arrows), with lesser
832 numbers of CD16+ CD206+ macrophages (arrowheads). Inset showing a higher magnification
833 of CD16+ CD11b+ CD206–macrophages (arrows). Asterix shows macrophages multifocally

834 surrounding small airways in GH99. White: DAPI (nuclei); Green: CD11b; Red: CD16; Blue:
835 CD206.
836
837 **Figure 4. CD11b+ neutrophils accumulate in lung of infected animals with severe disease.**
838 (**A**) Fluorescent immunohistochemistry in the lung of AGM and RM showing infiltration
839 of MPO+ neutrophils and MPO+ CD11b+ neutrophils. MPO and CD11b staining. White: DAPI
840 (nuclei); Green: CD11b; Red: MPO. The number of MPO positive cells (red, arrows) increases
841 in proportion to the severity of pulmonary disease from rare in the control (HK11), to mild in
842 FR04, moderate in GH99, and severe in NC34. Dual positive MPO+ CD11b+ positive cells
843 (arrowheads) are present in the most severely affected animals (NC34). (**B**) Mean number of
844 MPO+ cells, the standard deviation represents variability in the number of positive cells/area and
845 (**C**) and MPO+ CD11b+ per mm2 in lung necropsy.
846
847 **Figure 5. Lymphocytes infiltration in the lungs is associated with disease severity.** (**A**)
848 Histopathologic findings showing infiltration of lymphocytes in the lung of AGM (NC40 and
849 NC34) and RM (FR04 and GH99) with mild (NC40 and FR04), moderate (GH99), and severe
850 disease (NC34). (**B**) Frequency of NKG2a+ cells in the blood or (**C**) BAL of 4 AGM and 4 RM
851 at baseline, 2 weeks and 3 weeks post SARS-CoV-2 infection by flow cytometry. (**D**)
852 Representative flow cytometry plot showing decreased frequency of NGK2a+ cells in PBMCs
853 and increased frequency in BAL to baseline in at week 3 post SARS-CoV-2 infection respect to
854 baseline. One animal for each species is shown. (**E**) Decrease in the frequency of CXCR3+
855 NKG2a+ cells in the blood at 2 weeks, and 3 weeks post SARS-CoV-2 infection compared to the
856 baseline. (**F**) Absolute number of lymphocytes before and after infection. (**G**) tSNE plots

857 displaying kinetics of PD-1 expression (in red) on lymphocytic cell populations over time. (**H**)
858 Frequency of PD-1+ Th2 (CXCR3– CCR6–) CD4+ T cells is increased in RM and (**I**) in AGM
859 overtime following the infection. (**J**) Changes in the percentage of Th2 (purple), Th1 (blue) and
860 Th17 (grey) cells within the total PD-1+ CD4+ T cell population. (**K**) Significant increase in the
861 percentage of PD-1+ CD8+ T cells in BAL.
862
863 **Figure 5. Increased IL-6 in the absence of IL-10 is associated with disease progression.**
864 Levels of IL-6 and IL-10 in plasma overtime (pg/ml) **(A)** and (**B)** correlation between the ratio of
865 IL-10 to IL-6 levels measured in plasma and the ranking of disease severity or (**C**) with
866 pathology score**.** (**D**) Association between Kyn /Tryp ratio in plasma (pg/ml) and pathology
867 score. (**E**) Summary of immune events in lungs and blood of SARS-CoV-2 infected animals,
868 from the 1-acute phase 2- switch to Th2 type responses and 3- resolution phase.
869 **Table 1: Heterogeneous clinical and pathological outcomes following SARS-CoV-2 infection**

Animal ID	Clinical Findings	Clinical Score	Pathology Findings	Pathology Score	Ranking
NC34	Severe reduction in SpO_2, moderate tachypnea, and severe hypothermia just prior to euthanasia for severe respiratory distress at 8 days post infection. Less than 24 hours earlier, the only abnormality was a moderate reduction in SpO_2. Radiography appeared unremarkable until euthanasia when moderate to severe alveolar pattern with lobar sign and air bronchograms in right lung fields was observed.	9	Bronchointerstitial lung pattern in all lobes that was most severe in the right caudal lung lobe. Microscopically all lung lobes exhibited similar changes with the right caudal and right accessory lung lobe being the most severely affected. The lung lesions were comprised of diffuse alveolar damage with hyaline membrane formation, type II pneumocyte hyperplasia, and rare multinucleated giant syncytia. Some regions showed early evidence of organizing pneumonia and fibrosis.	19	1
NC33	Severe reduction in SpO_2, severe tachypnea, and severe hypothermia just prior to euthanasia for severe respiratory distress at 22 days post infection. Less than 24 hours earlier, the only abnormality was a mild reduction in SpO_2. Radiography appeared unremarkable until euthanasia when moderate to severe alveolar pattern in right middle/caudal lung fields and mild alveolar pattern left caudal lung fields were observed.	10	Severe diffuse alveolar damage of the right lower lung lobe. Other lobes exhibited suppurative alveolar infiltrate with lesser fibrin and edema. The right lung lobe contains peracute to acute lesions of necrosis, fibrin, and hemorrhage with minimal cellular infiltrate.	14	2
GH99	Transient cough beginning on 15 days post infection. Radiography showed significant changes at 11 days post infection which improved through 27 days post infection.	1	Severe bronchopneumonia of the right lower lung with granulomatous to pyogranulomatous inflammatory response.	10	3
NC38	Minor intermittent reductions in SpO_2	0	Mild interstitial pneumonia with low numbers of multinucleated giant cells and rare atypical pneumocyte hyperplasia.	8	4
HD09	Mild focal increase opacity ventral lung field at 11 days post infection.	1	Minimal to mild inflammation scattered throughout the lungs.	9	5
HB37	Intermittent mild to moderate pyrexia from 1-21 days post infection with mild dehydration from 14-21 days post infection.	1	Proliferative lymphocytic vasculitis and proliferative vasculopathy in the right middle lung lobe. Scattered interstitial inflammation throughout the remaining lung lobes.	5	6
FR04	Unremarkable	0	Bronchioles exhibited multifocal, mild mineralization.	6	7
NC40	Minor intermittent reductions in SpO_2	1	Minimal changes within lungs. Mild multifocal thickening of the alveolar septa in the right lower lobe associated with a mild inflammatory infiltrate.	4	8

870
871 Clinical findings are summarized for the duration of infection. Clinical scores, pathology findings, and
872 pathology scores reflect measurements at time of necropsy. Rankings were determined based on a

873 combination of the clinical findings and scores throughout the duration of infection and the pathology
874 findings and scores at time of necropsy (1 = severe; 8 = mild).
875 SpO_2 = oxygen saturation.
876

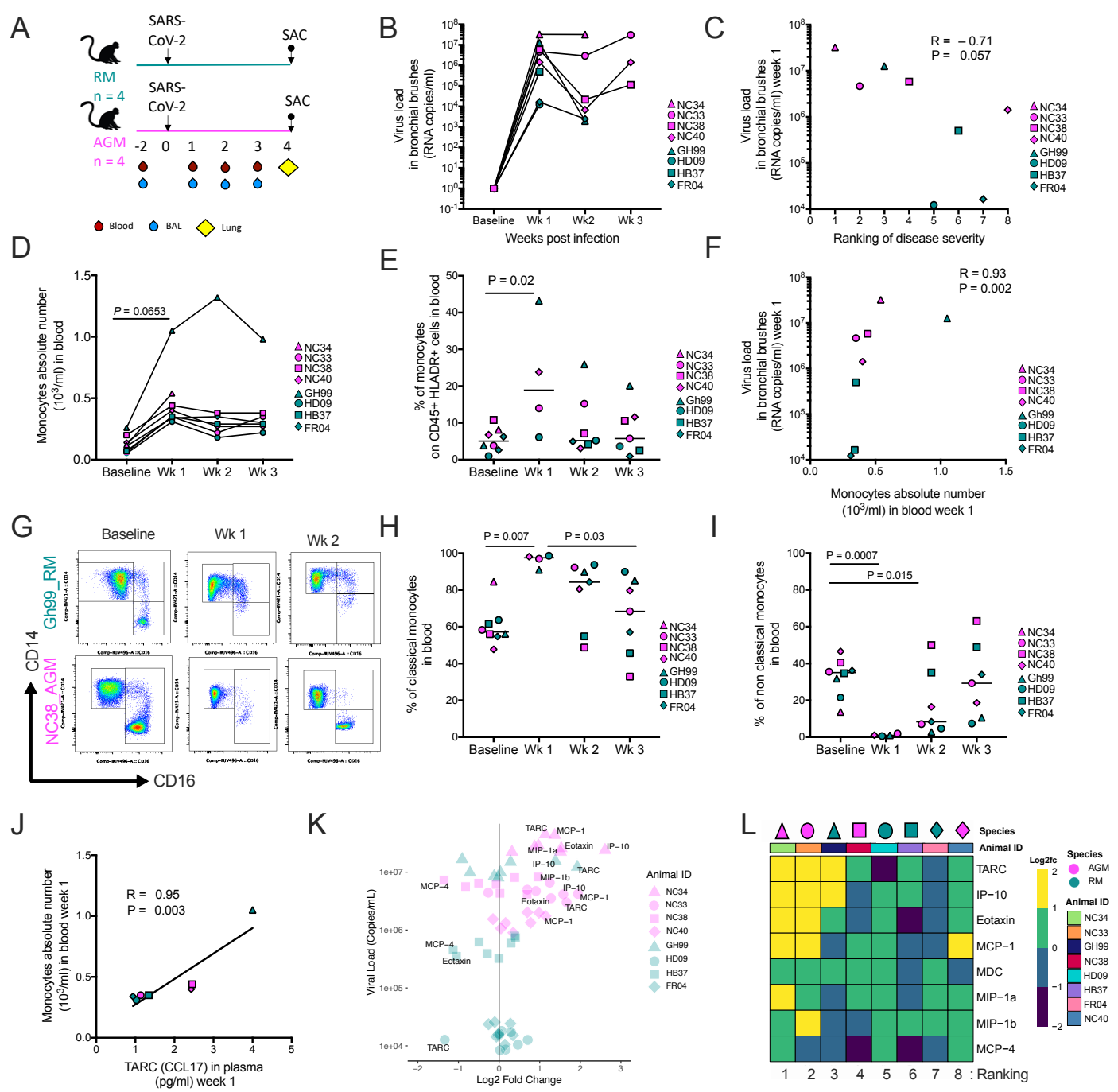
A
SARS-CoV-2
SAC
RM
n = 4
AGM
n = 4
-2 0 1 2 3 4
Blood
BAL
Lung
B
Virus load in bronchial brushes (RNA copies/ml)
Weeks post infection
Baseline
Wk 1
Wk2
Wk 3
NC34
NC33
NC38
NC40
GH99
HD09
HB37
FR04
C
R = −0.71
P = 0.057
Virus load in bronchial brushes (RNA copies/ml) week 1
Ranking of disease severity
D
P = 0.0653
Monocytes absolute number (10^3/ml) in blood
E
P = 0.02
% of monocytes on CD45+ HLADR+ cells in blood
F
R = 0.93
P = 0.002
Monocytes absolute number (10^3/ml) in blood week 1
G
Baseline
Wk 1
Wk 2
Gh99_RM
NC38_AGM
CD14
CD16
H
P = 0.007
P = 0.03
% of classical monocytes in blood
I
P = 0.0007
P = 0.015
% of non classical monocytes in blood
J
R = 0.95
P = 0.003
Monocytes absolute number (10^3/ml) in blood week 1
TARC (CCL17) in plasma (pg/ml) week 1
K
Viral Load (Copies/mL)
Log2 Fold Change
TARC
MCP−1
Eotaxin
IP−10
MIP−1a
MIP−1b
MCP−4
Animal ID
L
Species
Animal ID
Log2fc
AGM
RM
TARC
IP−10
Eotaxin
MCP−1
MDC
MIP−1a
MIP−1b
MCP−4
: Ranking

Figure 1

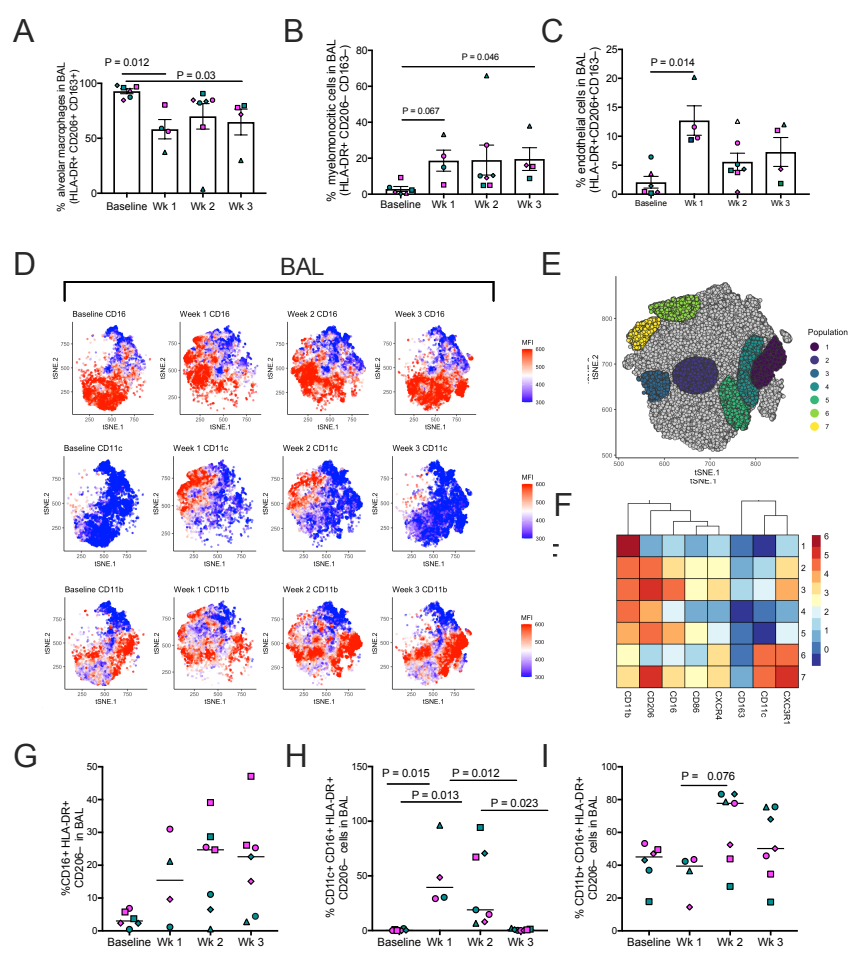
A
% alveolar macrophages in BAL (HLA-DR+ CD206+ CD163+)
P = 0.012
P = 0.03
Baseline
Wk 1
Wk 2
Wk 3
B
% myelomonocitic cells in BAL (HLA-DR+ CD206– CD163–)
P = 0.046
P = 0.067
C
% endothelial cells in BAL (HLA-DR+CD206+CD163–)
P = 0.014
D
BAL
Baseline CD16
Week 1 CD16
Week 2 CD16
Week 3 CD16
Baseline CD11c
Week 1 CD11c
Week 2 CD11c
Week 3 CD11c
Baseline CD11b
Week 1 CD11b
Week 2 CD11b
Week 3 CD11b
tSNE.1
tSNE.2
MFI
E
Population
F
CD11b
CD206
CD16
CD86
CXCR4
CD163
CD11c
CXC3R1
G
%CD16+ HLA-DR+ CD206– in BAL
H
% CD11c+ CD16+ HLA-DR+ CD206– cells in BAL
P = 0.015
P = 0.012
P = 0.013
P = 0.023
I
% CD11b+ CD16+ HLA-DR+ CD206– cells in BAL
P = 0.076

Figure 2

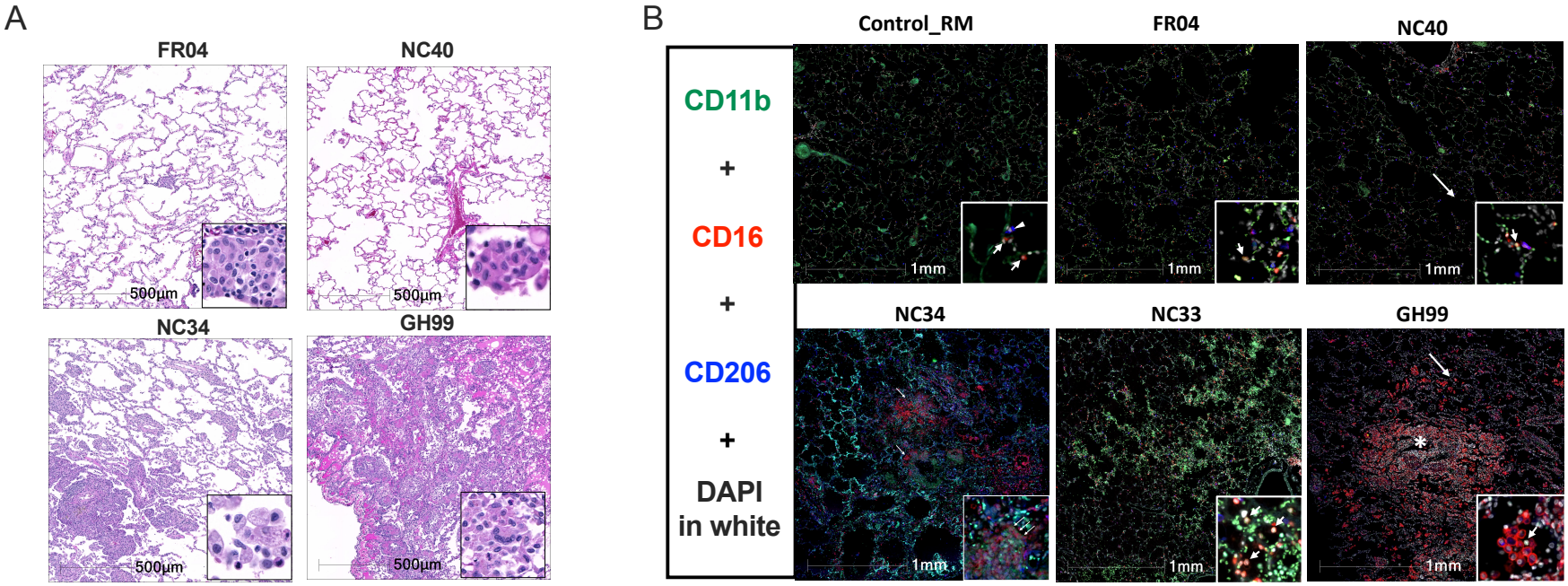
A
FR04
NC40
NC34
GH99
500µm
B
Control_RM
FR04
NC40
NC34
NC33
GH99
CD11b
+
CD16
+
CD206
+
DAPI
in white
1mm

Figure 3

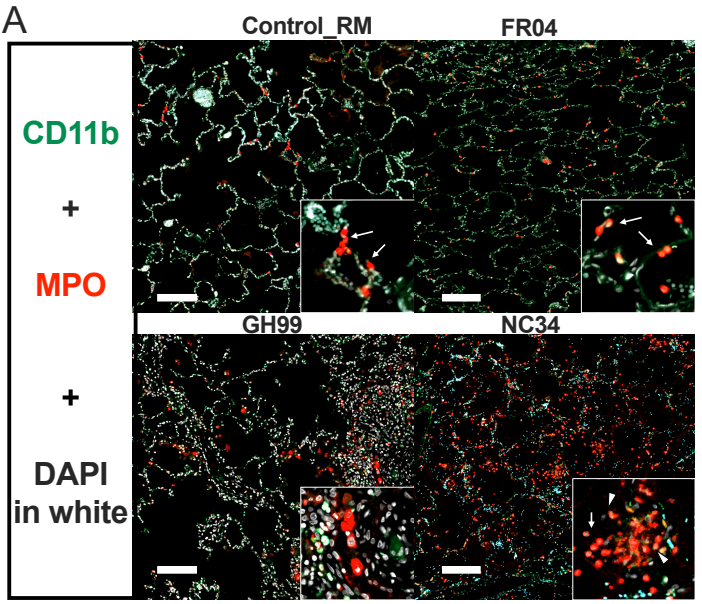
A
Control_RM
FR04
CD11b
+
MPO
+
DAPI
in white
GH99
NC34

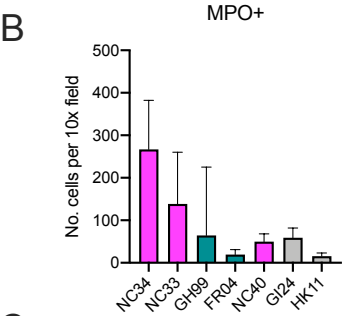
B
MPO+
No. cells per 10x field
500
400
300
200
100
0
NC34
NC33
GH99
FR04
NC40
GI24
HK11

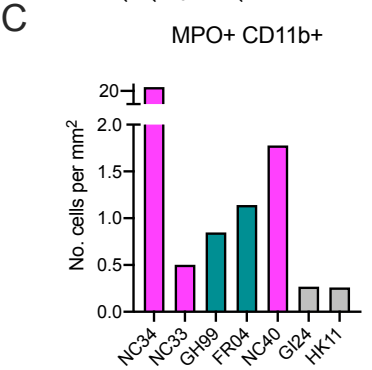
C
MPO+ CD11b+
No. cells per mm2
20
2.0
1.5
1.0
0.5
0.0
NC34
NC33
GH99
FR04
NC40
GI24
HK11

Figure 4

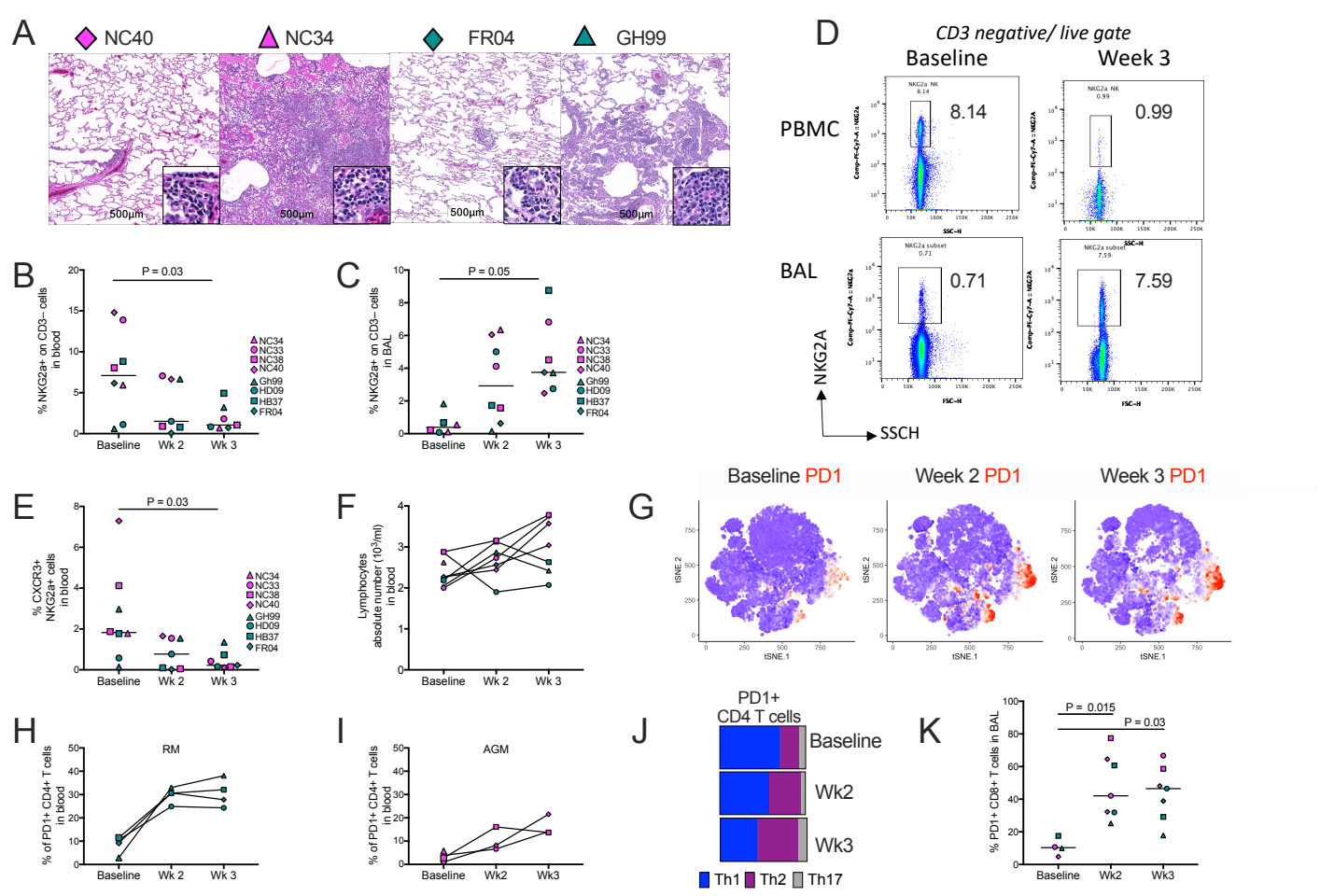
A
NC40
NC34
FR04
GH99
500µm
B
P = 0.03
% NKG2a+ on CD3− cells in blood
Baseline
Wk 2
Wk 3
NC34
NC33
NC38
NC40
Gh99
HD09
HB37
FR04
C
P = 0.05
% NKG2a+ on CD3− cells in BAL
D
CD3 negative/ live gate
Baseline
Week 3
PBMC
BAL
8.14
0.99
0.71
7.59
NKG2A
SSCH
E
P = 0.03
% CXCR3+ NKG2a+ cells in blood
F
Lymphocytes absolute number (10³/ml) in blood
G
Baseline PD1
Week 2 PD1
Week 3 PD1
tSNE.1
tSNE.2
H
RM
% of PD1+ CD4+ T cells in blood
I
AGM
Wk2
Wk3
J
PD1+ CD4 T cells
Baseline
Wk2
Wk3
Th1
Th2
Th17
K
P = 0.015
P = 0.03
% PD1+ CD8+ T cells in BAL

Figure 5

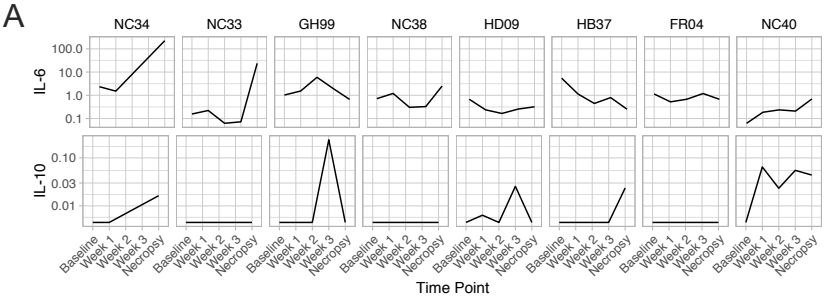
A
NC34
NC33
GH99
NC38
HD09
HB37
FR04
NC40
IL-6
100.0
10.0
1.0
0.1
IL-10
0.10
0.03
0.01
Baseline
Week 1
Week 2
Week 3
Necropsy
Time Point

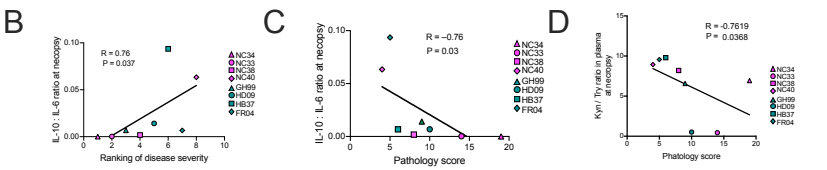
B
R = 0.76
P = 0.037
IL-10 : IL-6 ratio at necopsy
Ranking of disease severity
C
R = −0.76
P = 0.03
IL-10 : IL-6 ratio at necopsy
Pathology score
D
R = -0.7619
P = 0.0368
Kyn / Try ratio in plasma at necropsy
Phatology score
NC34
NC33
NC38
NC40
GH99
HD09
HB37
FR04

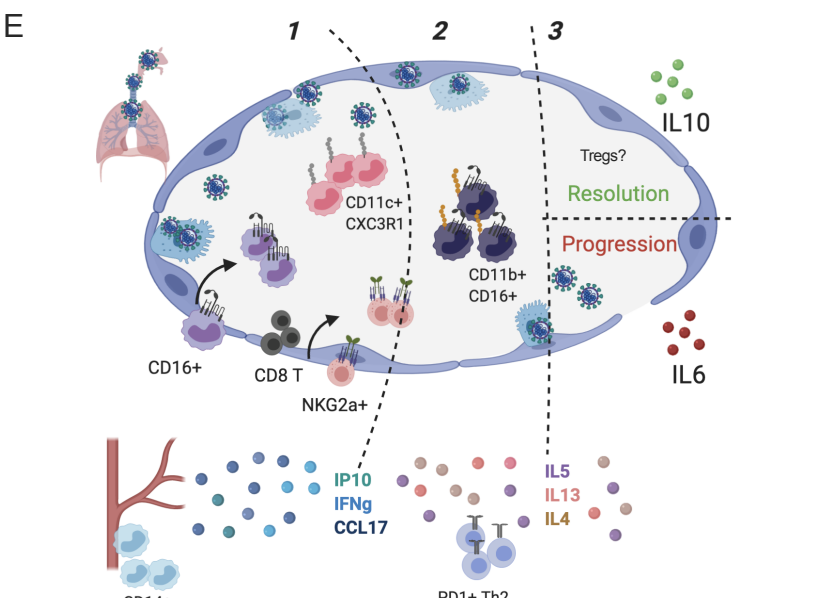
E
1
2
3
IL10
Tregs?
Resolution
Progression
CD11c+
CXC3R1
CD11b+
CD16+
CD16+
CD8 T
NKG2a+
IL6
IP10
IFNg
CCL17
IL5
IL13
IL4
CD14+
PD1+ Th2

Figure 6